# Analytic Formulation for Kinematics, Statics, and Shape Restoration of Multibackbone Continuum Robots Via Elliptic Integrals

**Kai Xu**
e-mail: kx2102@columbia.edu

**Nabil Simaan**[1]
Assistant Professor
e-mail: ns2236@columbia.edu

Department of Mechanical Engineering,
ARMA—Laboratory for Advanced Robotics and Mechanism Applications,
Columbia University,
New York, NY 10027

*This paper presents a novel and unified analytic formulation for kinematics, statics, and shape restoration of multiple-backbone continuum robots. These robots achieve actuation redundancy by independently pulling and pushing three backbones to carry out a bending motion of two-degrees-of-freedom (DoF). A solution framework based on constraints of geometric compatibility and static equilibrium is derived using elliptic integrals. This framework allows the investigation of the effects of different external loads and actuation redundancy resolutions on the shape variations in these continuum robots. The simulation and experimental validation results show that these continuum robots bend into an exact circular shape for one particular actuation resolution. This provides a proof to the ubiquitously accepted circular-shape assumption in deriving kinematics for continuum robots. The shape variations due to various actuation redundancy resolutions are also investigated. The simulation results show that these continuum robots have the ability to redistribute loads among their backbones without introducing significant shape variations. A strategy for partially restoring the shape of the externally loaded continuum robots is proposed. The simulation results show that either the tip orientation or the tip position can be successfully restored.* [DOI: 10.1115/1.4000519]

## 1 Introduction

Continuum robots (a term coined in Ref. [1]) have been the subject of extensive research due to their potential use in a wide range of applications [2–6]. Unlike articulated designs of snakelike robots, continuum robots substitute articulated spines with flexible members (often called backbones). These members may be elastomers [2], springs [7,8], bellows [4,5], flexures [9], or flexible beams [10–12]. Use of these flexible members presents various advantages in terms of reduced weight, obstacle avoidance, flexibility, safe interaction with unstructured environments, tolerance for geometric variations in grasped objects, and so on.

Continuum robots have a great potential for a variety of medical applications since they provide a safe and soft interaction with the human anatomy due to their inherent flexibility. Suzumori et al. [13] fabricated a flexible actuator driven by an electropneumatic system at various diameters as catheter tips, robotic hands, and snakelike manipulators. Haga et al. [14] fabricated continuum catheters using shape memory alloy (SMA) coils and etched SMA plates for actuation. Dario et al. [15] fabricated a steerable end effector for knee arthroscopy using four extensible SMA wires, while Asari et al. [16] used pneumatically actuated bellows to fabricate continuum robots for endoscopy and colonoscopy. The design of Ref. [7] using wire-actuated flexible spring for continuum robots was adapted for medical applications by Breedveld and Hirose [8] and Patronik et al. [17]. Breedveld and Hirose [8] designed a dexterous endoperiscope while Patronik et al. [17] recently developed the HeartLander robot for the minimally invasive therapy delivery to the surface of a beating heart. Peirs et al. [9] designed a surgical robot using a wire-actuated NiTi tube equipped with flexure joints as a flexible backbone. In addition, continuum robots have been investigated for use as steerable cannulas for image-guided drug delivery, biopsy, and brachytherapy [18–21].

Recently, Simaan et al. [11] presented a new type of continuum robot using multiple flexible backbones with a push-pull actuation. This design is a modification of the designs that use a single flexible backbone actuated by wires [22–24]. Figure 1(*c*) shows a prototype developed for Minimally Invasive Surgery (MIS) of the throat and the upper airways [25].

This type of continuum robot consists of several disks and four superelastic NiTi tubes as its backbones. As shown in Figs. 1(*a*)–1(*c*) and 2(*a*)–2(*c*), one *primary backbone* is centrally located and is glued to all the disks. Three identical *secondary backbones* are equidistant from each other and from the primary backbone. The secondary backbones are only attached to the end disk and can slide in appropriately toleranced holes in the spacer disks and in the base disk. Two consecutive disks form a subsegment of the robot. Each secondary backbone is actuated in a push-pull mode. A 2-DoF bending motion of the continuum robot is achieved through a simultaneous independent actuation of three secondary backbones (*actuation redundancy*).

In order to fully understand the characteristics of this type of continuum robot, the following topics need to be addressed.

- Kinematic and static modeling: given the desired orientation of the end disk, find the actuation lengths of the secondary backbones, as well as obtain the internal load distribution within the robot structure.
- Stiffness modeling: given an external wrench acting on the end disk, find the variation in its position and orientation.

Among the aforementioned examples of continuum robots, Refs. [22–24] presented kinematics, manipulability, control, and

[1]Corresponding author.

Contributed by the Mechanisms and Robotics Committee of ASME for publication in the JOURNAL OF MECHANISMS AND ROBOTICS. Manuscript received November 7, 2008; final manuscript received July 14, 2009; published online November 24, 2009. Assoc. Editor: J. Michael McCarthy.

  

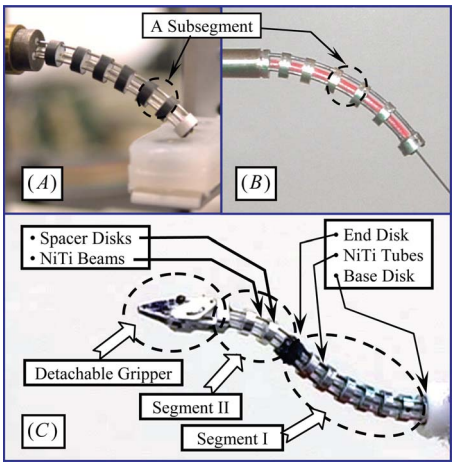


**Fig. 1 Continuum robots with actuation redundancy: (*a*) a Ø7.5 mm one, (*b*) a Ø4.2 mm one, and (*c*) a two-segment robot**

compliance analysis for cable-actuated continuum robots with one flexible backbone. In these works, it was assumed that each flexible segment bends into a circular shape. To address the issue of a circular bending assumption, Li and Rhan [26] provided a numerical solution for the nonlinear elasticity equations governing the shape of a planar cable-actuated continuum robot in addition to presenting modeling errors. However, these results do not apply here due to the structural differences.

This paper presents an analytic formulation for kinematics, statics, and shape restoration for this type of continuum robot. The contributions include:

- A novel and unified analytic modeling framework is formulated for continuum robots with multiple flexible backbones. This framework solves kinematics, statics, and stiffness of the entire continuum robot via elliptic integrals.
- The modeling framework is used to investigate the effects of different actuation redundancy resolutions on shape variations of the multibackbone continuum robot. A method for actuating the backbones in order to partially restore the shape of an externally loaded continuum robot is presented.

The approach taken in this paper is as follows: elliptic integrals are used to express the backbones' deflected shapes within a subsegment of the continuum robot; static equilibrium is formulated such that both the kinematics problem and the stiffness problem can be solved within the same framework; results for the distal subsegment are propagated to adjacent subsegments; the results for both the *actuation redundancy resolutions* and the *shape restoration* are then obtained for the entire robot.

Although finite element methods could also be used to solve these problems, elliptic integrals are chosen for two major advantages: (i) the formulation and the related partial derivatives are obtained analytically, which allows a fast convergence; this implies the possibility of extending the presented results for future real-time applications (e.g., online shape restoration and actuation compensation); and (ii) the circular bending shape of the robot in one particular actuation mode is analytically proven, while the shape can only be observed to numerically approach a circular arc if a finite element method is used.

Section 2 summarizes coordinate systems and modeling assumptions. Using elliptic integrals, Sec. 3 presents a unified kinestatic formulation framework for solving kinematics, statics, and shape restoration. Section 4 presents solutions for kinematics and statics of the continuum robot under different actuation modes as well as validates an approximate model through simulations and experiments. Section 5 presents solutions of shape restoration and Sec. 6 provides conclusions.

## 2 Coordinate Systems and Modeling Assumptions

**2.1 Coordinate Systems.** The following coordinate systems (shown in Figs. 2(*a*)–2(*c*)) are defined to help derive and describe the kinematics and statics of the continuum robot.

- *Base disk coordinate system* (BDS) $\{\hat{\mathbf{x}}_b, \hat{\mathbf{y}}_b, \hat{\mathbf{z}}_b\}$ is attached to the base disk, whose *XY* plane is defined to coincide with the upper surface of the base disk and its origin is at the center of the base disk. $\hat{\mathbf{x}}_b$ points from the center of the base disk to the first secondary backbone while $\hat{\mathbf{z}}_b$ is normal to the base disk. The three secondary backbones are numbered according to the definition of $\delta_i$.
- *Bending plane coordinate system* (BPS) $\{\hat{\mathbf{x}}_1, \hat{\mathbf{y}}_1, \hat{\mathbf{z}}_1\}$ is defined such that the continuum robot bends in its *XZ* plane, with its origin coinciding with the origin of BDS. When the robot is in a straight configuration, $\hat{\mathbf{x}}_1$ is defined by the commanded (desired) instantaneous linear velocity of the end disk.
- *End disk coordinate system* (EDS) $\{\hat{\mathbf{x}}_e, \hat{\mathbf{y}}_e, \hat{\mathbf{z}}_e\}$ is obtained from BPS by a rotation about $\hat{\mathbf{y}}_1$ such that $\hat{\mathbf{z}}_1$ becomes the backbone tangent at the end disk. The origin of EDS is also translated to the center of the end disk.
- *Gripper coordinate system* (GCS) $\{\hat{\mathbf{x}}_g, \hat{\mathbf{y}}_g, \hat{\mathbf{z}}_g\}$ is attached to an imaginary gripper affixed to the end disk. $\hat{\mathbf{x}}_g$ points from the center of the end disk to the first secondary backbone and $\hat{\mathbf{z}}_g$ is normal to the end disk. GCS is obtained by a right-handed rotation about $\hat{\mathbf{z}}_e$.
- *Subsegment coordinate system* (SPS) $\{\hat{\mathbf{x}}_s^{(t)}, \hat{\mathbf{y}}_s^{(t)}, \hat{\mathbf{z}}_s^{(t)}\}$ (*t*

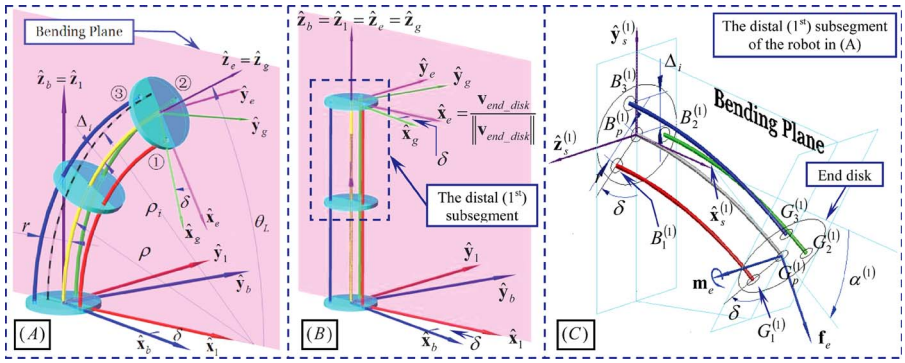


**Fig. 2 Kinematics nomenclature with the definition of $\delta$ for (*a*) a bent robot, (*b*) a straight robot, and (*c*) the distal subsegment**

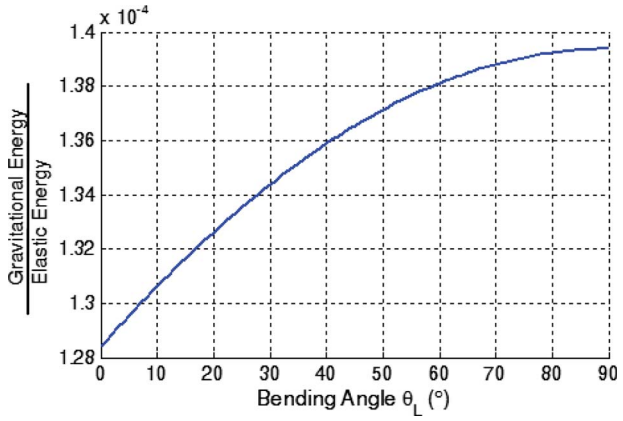


**Fig. 3 Gravitational energy over the elastic energy ratio**

$=1,2,\ldots,n$, numbering first from the distal end) is defined to facilitate solving the kinematics and statics for each subsegment. Its $XY$ plane is aligned with the robot bending plane, while its $YZ$ plane is centered at the corresponding spacer disk of the subsegment. $\{\hat{\mathbf{x}}_s^{(1)},\hat{\mathbf{y}}_s^{(1)},\hat{\mathbf{z}}_s^{(1)}\}$ is shown in Fig. 2(*c*) for the distal subsegment.

**2.2 Modeling Assumptions.** The following modeling assumptions are made.

- The superelastic material NiTi is assumed to have linear and isotropic relations between stain and stress [27] in the presented robot. The backbones behave like Euler–Bernoulli beams.
- The robot is under static equilibrium.
- According to Fig. 3, gravity is ignored in the analysis, since the gravitational potential energy is less than 0.014% of the elastic deformation energy for a small continuum robot. This plot was generated for a vertically placed robot using numerical values from Table 1. Its shape is assumed circular (density of NiTi is 6.2 g/cm$^3$, each disk weighs 0.32 g).
- The robot disks are thin and rigid. Friction between the backbones and the disks is neglected.
- The primary and the secondary backbones are always perpendicular to the base, the spacer, and the end disks. The perpendicularity of the backbones with respect to the spacer disks will be validated later in Sec. 4.1 where results for adjacent subsegments are obtained.

## 3 Kinestatic Formulation

This section introduces a unified formulation framework. Within one subsegment made up of four elastic beams and two disks, there are constraints for the static equilibrium of the robot disks, as well as constraints for the geometric compatibility between the disks and the backbones. Formulation of these two sets of constraints will be used in later sections to solve for kinematics, statics, and shape restoration of the robot.

As shown in Fig. 2(*a*), three secondary backbones are actuated in a push-pull mode to bend the continuum robot to a desired tip angle (specified by $\theta_L$) in a desired bending plane (specified by $\delta$). In order to solve the kinematics and statics for the entire robot, analysis was first applied to the distal subsegment of the robot, as

**Table 1 Numerical values of the robot variables**

| | | | |
|---|---|---|---|
| $L_{sp}^{(1)}=30$ mm | $r=3$ mm | $\delta=15$ deg | $E_p=E_s=62$ GPa |
| $\alpha^{(1)}=30$ deg | $d_{op}=d_{oi}=0.889$ mm | | $d_{ip}=d_{ii}=0.762$ mm |

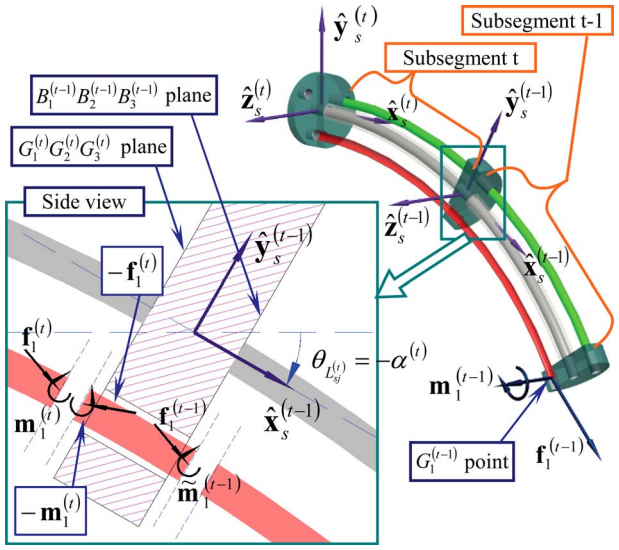


**Fig. 4 Static equilibrium of a spacer disk**

shown in Fig. 2(*c*). Results for the distal (first) subsegment were then propagated to adjacent subsegments to form the solution for the entire robot.

An implicit assumption adopted here is that all of the backbones bend in a planar manner: the primary backbone bends in the bending plane while the secondary backbones bend in planes parallel to the bending plane. Solutions obtained in Sec. 4.1 will validate this assumption. This assumption eventually holds because in addition to neglecting the gravity the external wrench is assumed in the bending plane.

**3.1 Static Equilibrium Constraints.** The analysis for each subsegment involves four backbones and two disk planes ($B_1^{(t)}B_2^{(t)}B_3^{(t)}$ and $G_1^{(t)}G_2^{(t)}G_3^{(t)}$). Figure 2(*c*) shows the first subsegment, while Fig. 4 shows two consecutive subsegments. For the $t$th subsegment, there is a force $\mathbf{f}_p^{(t)}$ and a moment $\mathbf{m}_p^{(t)}$ acting on the primary backbone at point $G_p^{(t)}$ as well as force $\mathbf{f}_i^{(t)}$ and moment $\mathbf{m}_i^{(t)}$ acting on the $i$th secondary backbone at point $G_i^{(t)}$ by disk $G_1^{(t)}G_2^{(t)}G_3^{(t)}$. For the first (distal) subsegment, the robot disk $G_1^{(1)}G_2^{(1)}G_3^{(1)}$ could also be subject to an external force $\mathbf{f}_e$ and a moment $\mathbf{m}_e$.

Referring to Fig. 2(*c*), static equilibrium of the end disk $G_1^{(1)}G_2^{(1)}G_3^{(1)}$ in the first subsegment gives

$$\mathbf{c}_s^{(1)}=\begin{bmatrix}\sum_{i=1}^{3}(-\mathbf{f}_i^{(1)})+(-\mathbf{f}_p^{(1)})+\mathbf{f}_e\\ \sum_{i=1}^{3}(-\mathbf{m}_i^{(1)}+\overline{G_p^{(1)}G_i^{(1)}}\times(-\mathbf{f}_i^{(1)}))+(-\mathbf{m}_p^{(1)})+\mathbf{m}_e\end{bmatrix}=\mathbf{0} \tag{1}$$

where $\overline{G_p^{(1)}G_i^{(1)}}$ is the vector from point $G_p^{(1)}$ to $G_i^{(1)}$.

Equation (1) states the static equilibrium of the end disk, which is glued to all of the backbones. In contrast, a spacer disk is only glued to the primary backbone while the secondary backbones can slide in its holes.

Referring to the side view of Fig. 4, the spacer disk with $\{\hat{\mathbf{x}}_s^{(t-1)},\hat{\mathbf{y}}_s^{(t-1)},\hat{\mathbf{z}}_s^{(t-1)}\}$ is under static equilibrium. $-\mathbf{f}_j^{(t)}$ and $-\mathbf{m}_j^{(t)}$ are the force and moment exerted on the disk by the backbones in the subsegment $t$, while $\mathbf{f}_j^{(t-1)}$ and $\tilde{\mathbf{m}}_j^{(t-1)}$ are the force and moment exerted on the disk by the backbones in the subsegment $t-1$. Since the secondary backbone can slide in the direction of $\hat{\mathbf{x}}_s^{(t-1)}$, $-\mathbf{f}_i^{(t)}$ and $\mathbf{f}_i^{(t-1)}$ need to balance each other in this direction. In

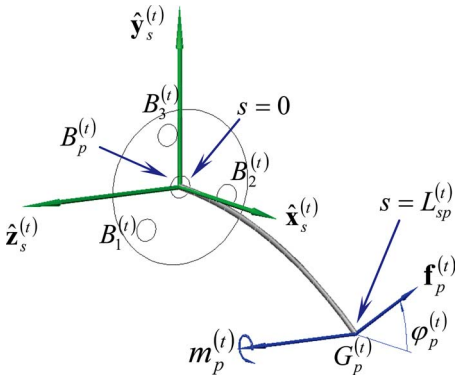


**Fig. 5 Deformed primary backbone of the *t*th subsegment as a result of force $\mathbf{f}_p^{(t)}$ and moment $\mathbf{m}_p^{(t)}$**

addition, if $-\mathbf{f}_i^{(t)}$ counteracts $\mathbf{f}_i^{(t-1)}$ $(i=1,2,3)$, $-\mathbf{f}_p^{(t)}$ will also counteract $\mathbf{f}_p^{(t-1)}$. Otherwise the force balance in the direction of $\hat{\mathbf{x}}_s^{(t-1)}$ will not hold. Hence, the static equilibrium constraints for the spacer disk are formulated as follows:

$$\mathbf{c}_s^{(t)}=\begin{bmatrix} -\mathbf{f}_j^{(t)}\cdot\hat{\mathbf{x}}_s^{(t-1)}+\mathbf{f}_j^{(t-1)}\cdot\hat{\mathbf{x}}_s^{(t-1)}, \quad j=1,2,3,p \\ \left(\sum_{i=1}^{3}(-\mathbf{f}_i^{(t)})+(-\mathbf{f}_p^{(t)})+\sum_{i=1}^{3}(\mathbf{f}_i^{(t-1)})+\mathbf{f}_p^{(t-1)}\right)\cdot\hat{\mathbf{y}}_s^{(t-1)} \\ \sum_{i=1}^{3}\left(\begin{matrix}-\mathbf{m}_i^{(t)}+\overline{G_p^{(t)}G_i^{(t)}}\times(-\mathbf{f}_i^{(t)}) \\ +\tilde{\mathbf{m}}_i^{(t-1)}+\overline{G_p^{(t-1)}G_i^{(t-1)}}\times\mathbf{f}_i^{(t)}\end{matrix}\right)-\mathbf{m}_p^{(t)}+\tilde{\mathbf{m}}_p^{(t-1)} \end{bmatrix}=\mathbf{0} \tag{2}$$

where $t=2,3,\ldots,n$. In the equilibrium, $\mathbf{f}_j^{(t-1)}$ and $\mathbf{m}_j^{(t-1)}$ are translated from $G_j^{(t-1)}$ to $B_j^{(t-1)}$, $\mathbf{f}_j^{(t-1)}$ remains the same, and $\tilde{\mathbf{m}}_j^{(t-1)}=\mathbf{m}_j^{(t-1)}+\overline{B_j^{(t)}G_j^{(t)}}\times\mathbf{f}_j^{(t-1)}$. The second row indicates the force balance in the direction of $\hat{\mathbf{y}}_s^{(t-1)}$ and the third row indicates the moment balance.

Please note that $\mathbf{f}_p^{(t)}$, $\mathbf{m}_p^{(t)}$, $\mathbf{f}_i^{(t)}$, $\mathbf{m}_i^{(t)}$, $\hat{\mathbf{x}}_s^{(t)}$, $\hat{\mathbf{y}}_s^{(t)}$, and $\hat{\mathbf{z}}_s^{(t)}$ $(t=1,2,\ldots,n)$ are different vectors for the $n$ subsegments in the robot. They have different forms when expressed in different coordinates. For the manipulations such as those in Eqs. (1) and (2), these vectors need to be expressed in one consistent coordinate system. According to the planar bending assumption mentioned before, $\mathbf{f}_j^{(t)}$ and $\mathbf{m}_j^{(t)}$ assume the following form in $\{\hat{\mathbf{x}}_s^{(t)},\hat{\mathbf{y}}_s^{(t)},\hat{\mathbf{z}}_s^{(t)}\}$, with $f_j^{(t)}\geq 0$:

$$\mathbf{f}_j^{(t)}=\begin{bmatrix} f_j^{(t)}\cos\varphi_j^{(t)} & f_j^{(t)}\sin\varphi_j^{(t)} & 0\end{bmatrix}^T \tag{3}$$

$$\mathbf{m}_j^{(t)}=\begin{bmatrix} 0 & 0 & m_j^{(t)}\end{bmatrix}^T \tag{4}$$

where $f_j^{(t)}$ is the amplitude and $\varphi_j^{(t)}$ is the angle indicating the force direction.

Since only the planar bending problem of a thin beam has a closed-form expression, $\mathbf{f}_e$ and $\mathbf{m}_e$ assume the following forms in $\{\hat{\mathbf{x}}_s^{(1)},\hat{\mathbf{y}}_s^{(1)},\hat{\mathbf{z}}_s^{(1)}\}$:

$$\mathbf{f}_e=\begin{bmatrix} f_{ex} & f_{ey} & 0\end{bmatrix}^T \quad \text{and} \quad \mathbf{m}_e=\begin{bmatrix} 0 & 0 & m_e\end{bmatrix}^T \tag{5}$$

**3.2 Geometric Compatibility Constraints.** Besides the statics equilibrium constraints formulated in Eqs. (1) and (2), there also exist geometry compatibility constraints. According to Eq. (3) from Ref. [28] or a similar derivation in Refs. [29–32], the differential equation governing the planar shape of the primary backbone and the *i*th secondary backbone can be written as in Eq. (6) $(j=1,2,3,p)$. The equation is written in $\{\hat{\mathbf{x}}_s^{(t)},\hat{\mathbf{y}}_s^{(t)},\hat{\mathbf{z}}_s^{(t)}\}$ and the minus sign comes from the downward deflection, as shown in Figs. 2(*c*) and 5. $\theta_{L_{sj}^{(t)}}$ is the deflection angle at the distal tip of the backbones in the *t*th subsegment. Integrating Eq. (6) along the backbones leads to Eqs. (7)–(9)

$$ds=\sqrt{\frac{E_jI_j}{2}}\frac{-d\theta}{\sqrt{a_j^{(t)}-f_j^{(t)}\cos(\theta-\varphi_j^{(t)})}} \tag{6}$$

where $a_j^{(t)}=(m_j^{(t)})^2/(2E_jI_j)+f_j^{(t)}\cos(\theta_{L_{sj}^{(t)}}-\varphi_j^{(t)})$

$$\int_0^{L_{sj}^{(t)}}ds=\sqrt{\frac{E_jI_j}{2}}\mathrm{I}_{1j}^{(t)} \tag{7}$$

where $\mathrm{I}_{1j}^{(t)}\equiv\int_0^{\theta_{L_{sj}^{(t)}}}\frac{-d\theta}{\sqrt{a_j^{(t)}-f_j^{(t)}\cos(\theta-\varphi_j^{(t)})}}$

$$\int_0^{L_{sj}^{(t)}}\cos\theta ds=\sqrt{\frac{E_jI_j}{2}}\mathrm{Int}_{cj}^{(t)} \tag{8}$$

$$\int_0^{L_{sj}^{(t)}}\sin\theta ds=\sqrt{\frac{E_jI_j}{2}}\mathrm{Int}_{sj}^{(t)} \tag{9}$$

where $\mathrm{Int}_{cj}^{(t)}\equiv\int_0^{\theta_{L_{sj}^{(t)}}}\frac{-\cos\theta d\theta}{\sqrt{a_j^{(t)}-f_j^{(t)}\cos(\theta-\varphi_j^{(t)})}}$

and $\mathrm{Int}_{sj}^{(t)}\equiv\int_0^{\theta_{L_{sj}^{(t)}}}\frac{-\sin\theta d\theta}{\sqrt{a_j^{(t)}-f_j^{(t)}\cos(\theta-\varphi_j^{(t)})}}$

as well as $\int_0^{L_{sj}^{(t)}}\cos\theta ds=(\overline{B_j^{(t)}G_j^{(t)}})|_x$ and $\int_0^{L_{sj}^{(t)}}\sin\theta ds=(\overline{B_j^{(t)}G_j^{(t)}})|_y$ while $|_x$ and $|_y$ stand for the $X$ and the $Y$ coordinates.

According to Fig. 2(*c*), since the disk $G_1^{(t)}G_2^{(t)}G_3^{(t)}$ is rigid and is perpendicular to all backbones, the value of $\theta_{L_{sj}^{(t)}}$ and the geometric compatibility constraints are given in Eqs. (10) and (11), respectively

$$\theta_{L_{sj}^{(t)}}=-\alpha^{(t)}, \quad j=1,2,3,p \tag{10}$$

$$(\overline{B_p^{(t)}B_i^{(t)}}+\overline{B_i^{(t)}G_i^{(t)}})|_{x,y}=(\overline{B_p^{(t)}G_p^{(t)}}+\overline{G_p^{(t)}G_i^{(t)}})|_{x,y} \tag{11}$$

where $\overline{B_p^{(t)}B_i^{(t)}}$, $\overline{B_i^{(t)}G_i^{(t)}}$, $\overline{B_p^{(t)}G_p^{(t)}}$, and $\overline{G_p^{(t)}G_i^{(t)}}$ are all vectors in $\{\hat{\mathbf{x}}_s^{(t)},\hat{\mathbf{y}}_s^{(t)},\hat{\mathbf{z}}_s^{(t)}\}$. The $X$ and $Y$ components are the only active constraints because the primary and secondary backbones bend in parallel planes.

The geometric compatibility constraints of Eq. (11) can be rewritten as below, with details in Appendix A

$$\mathbf{c}_c^{(t)}=\mathbf{0}=\begin{bmatrix} \sqrt{\frac{E_pI_p}{2}}\mathrm{Int}_{cp}^{(t)}-\sqrt{\frac{E_1I_1}{2}}\mathrm{Int}_{c1}^{(t)}-r\sin\alpha^{(t)}\cos\delta_1 \\ \sqrt{\frac{E_pI_p}{2}}\mathrm{Int}_{sp}^{(t)}-\sqrt{\frac{E_1I_1}{2}}\mathrm{Int}_{s1}^{(t)}-r\cos\delta_1(\cos\alpha^{(t)}-1) \\ \sqrt{\frac{E_pI_p}{2}}\mathrm{Int}_{cp}^{(t)}-\sqrt{\frac{E_2I_2}{2}}\mathrm{Int}_{c2}^{(t)}-r\sin\alpha^{(t)}\cos\delta_2 \\ \sqrt{\frac{E_pI_p}{2}}\mathrm{Int}_{sp}^{(t)}-\sqrt{\frac{E_2I_2}{2}}\mathrm{Int}_{s2}^{(t)}-r\cos\delta_2(\cos\alpha^{(t)}-1) \\ \sqrt{\frac{E_pI_p}{2}}\mathrm{Int}_{cp}^{(t)}-\sqrt{\frac{E_3I_3}{2}}\mathrm{Int}_{c3}^{(t)}-r\sin\alpha^{(t)}\cos\delta_3 \\ \sqrt{\frac{E_pI_p}{2}}\mathrm{Int}_{sp}^{(t)}-\sqrt{\frac{E_3I_3}{2}}\mathrm{Int}_{s3}^{(t)}-r\cos\delta_3(\cos\alpha^{(t)}-1) \end{bmatrix} \tag{12}$$

If $f_j^{(t)}=0$, the integrals of $\mathrm{I}_{1j}^{(t)}$, $\mathrm{Int}_{cj}^{(t)}$, and $\mathrm{Int}_{sj}^{(t)}$ can be directly derived from Eqs. (7)–(9), using Eq. (10), $j=1,2,3,p$

$$\mathrm{I}_{1j}^{(t)} = \sqrt{2E_jI_j}\alpha^{(t)}/|m_j^{(t)}| \tag{13}$$

$$\mathrm{Int}_{cj}^{(t)} = \sqrt{2E_jI_j}\,\sin\,\alpha^{(t)}/|m_j^{(t)}| \tag{14}$$

$$\mathrm{Int}_{sj}^{(t)} = \sqrt{2E_jI_j}(\cos\,\alpha^{(t)} - 1)/|m_j^{(t)}| \tag{15}$$

If $f_j^{(t)} > 0$, the integrals of $\mathrm{I}_{1j}^{(t)}$, $\mathrm{Int}_{cj}^{(t)}$, and $\mathrm{Int}_{sj}^{(t)}$ can be analytically expressed using elliptic integrals. Derivation details are listed in Appendix B with results summarized below

$$\mathrm{Int}_{cj}^{(t)} = \cos\,\varphi_j^{(t)}\mathrm{I}_{cj}^{(t)} + \sin\,\varphi_j^{(t)}\mathrm{I}_{sj}^{(t)} \tag{16}$$

$$\mathrm{Int}_{sj}^{(t)} = \sin\,\varphi_j^{(t)}\mathrm{I}_{cj}^{(t)} - \cos\,\varphi_j^{(t)}\mathrm{I}_{sj}^{(t)} \tag{17}$$

where $\mathrm{I}_{1j}^{(t)}$ and $\mathrm{I}_{cj}^{(t)}$ are listed in Table 2 and

$$\mathrm{I}_{sj}^{(t)} = \frac{2}{f_j^{(t)}}\left(\frac{|m_j^{(t)}|}{\sqrt{2E_jI_j}} - \sqrt{a_j^{(t)} - f_j^{(t)}\cos\,\varphi_j^{(t)}}\right) \tag{18}$$

where $a_j^{(t)} = (m_j^{(t)})^2/(2E_jI_j) + f_j^{(t)}\cos(\alpha^{(t)} + \varphi_j^{(t)})$, which is rewritten from $a_j^{(t)}$ in Eq. (6) by using Eq. (10).

In Table 2, $F(z,k)$ and $E(z,k)$ are the incomplete elliptic integrals of the first kind and the second kind, respectively. They are defined as the following:

$$F(z,k) = \int_0^z \frac{d\theta}{\sqrt{1 - k^2\,\sin^2\,\theta}} \tag{19}$$

$$E(z,k) = \int_0^z \sqrt{1 - k^2\,\sin^2\,\theta}\,d\theta \tag{20}$$

Results of Eqs. (25)–(28) are directly based on the equations of 289.00, 289.03, 293.07, 331.01, 290.00, 290.04, 291.00, 291.03, 315.02, and 318.02 from Ref. [33]. In Table 2, the expressions for $\mathrm{I}_{1j}^{(t)}$ and $\mathrm{I}_{cj}^{(t)}$ are listed for four different scenarios because the aforementioned equations have their valid input value ranges.

## 4 Kinematics

The continuum robot's kinematics can be presented more conveniently by using a configuration variable $\boldsymbol{\Psi}$, as defined in the Nomenclature. Its instantaneous direct kinematics from the configuration space $\boldsymbol{\Psi}$ to the task space $\mathbf{x}$, and the instantaneous inverse kinematics from the configuration space $\boldsymbol{\Psi}$ to the joint space $\mathbf{q}$ are then given by

$$\dot{\mathbf{x}} = \mathbf{J}_{\mathbf{x}\boldsymbol{\psi}}\dot{\boldsymbol{\Psi}} \tag{21}$$

$$\dot{\mathbf{q}} = \mathbf{J}_{\mathbf{q}\boldsymbol{\psi}}\dot{\boldsymbol{\Psi}} \tag{22}$$

where both $\mathbf{J}_{\mathbf{x}\boldsymbol{\Psi}}$ and $\mathbf{J}_{\mathbf{q}\boldsymbol{\Psi}}$ depend on the actual shape of the backbones of the continuum robot.

**4.1 Actuation Redundancy Resolution.** With the analysis formulated in Sec. 3 the inverse kinematics problem of bending the distal subsegment to a specific angle $\alpha^{(1)}$ under different actuation modes can be written as a constrained optimization problem

$$\mathbf{x}_a^{(1)} = \arg\,\min((\mathbf{f}_{123p} - \mathbf{f}_{\mathrm{user}})^T\mathbf{W}(\mathbf{f}_{123p} - \mathbf{f}_{\mathrm{user}})) \tag{23}$$

$$\text{subject to:}\begin{cases}\begin{bmatrix}\mathbf{c}_s^{(1)}\\ \mathbf{c}_c^{(1)}\end{bmatrix} = \mathbf{0}\\ \sqrt{E_pI_p/2}\mathrm{I}_{1p}^{(1)} - L_{sp}^{(1)} = 0\end{cases} \tag{24}$$

where $\mathbf{x}_a^{(t)} \in \Re^{12\times 1} = [f_1^{(t)}\ f_2^{(t)}\ f_3^{(t)}\ f_p^{(t)}\ \varphi_1^{(t)}\ \varphi_2^{(t)}\ \varphi_3^{(t)}\ \varphi_p^{(t)}\ m_1^{(t)}\ m_2^{(t)}\ m_3^{(t)}\ m_p^{(t)}]^T$ and $\mathbf{f}_{123p}^{(t)} = [f_1^{(t)}\ f_2^{(t)}\ f_3^{(t)}\ f_p^{(t)}]^T$. $f_j^{(t)}$, $\varphi_j^{(t)}$, and $m_j^{(t)}$ are from Eqs. (3) and (4). The first two sets of constraints are defined in Eqs. (1) and (12), while the third set of constraints states the length of the primary backbone equals its predetermined value.

In Eq. (23), $\mathbf{f}_{\mathrm{user}} = [f_{1\_\mathrm{user}}\ f_{2\_\mathrm{user}}\ f_{3\_\mathrm{user}}\ f_{p\_\mathrm{user}}]^T$ is a user specified target value for the backbone loads while $\mathbf{W}$ is a weight matrix.

The constrained minimization problem in Eq. (23) can be treated by seeking the solutions of its Karush–Kuhn–Tucker (KKT) equations, as described in Ref. [34]. The KKT equations of this optimization problem are solved using sequential quadratic programming (SQP) as detailed in Refs. [34–36]. The actual implementation uses MATLAB 2008A®'s optimization toolbox. Since the formulation of the KKT equations involves the partial derivatives of the constraints in Eq. (24), the analytical expressions of these partial derivatives are derived, with some details presented in Appendix C.

*Actuation mode 1*. Minimal force on the primary backbone. The minimization problem of Eq. (23) is solved for $\mathbf{f}_{\mathrm{user}} = [0\ 0\ 0\ 0]^T$ and $\mathbf{W} = \mathrm{diag}(0,0,0,1)$. Numerical values of the structure of the continuum robot are from the Nomenclature. Results are from Table 1 as well as plotted in Figs. 6 and 7. Computation was conducted on a 2.4 GHz duo core laptop with an average convergence time of 95–120 ms. Figure 7 registers and overlays the theoretic results to an image of an actuated subsegment under a microscope (shown in Fig. 15). The predicted shapes of the backbones fit the actual shape very well (the maximal discrepancy between the actual shape and the predicted shape is 0.09 mm). Hypothetical circular arcs are also drawn in dashed lines to show the shape deviation between the actual backbones and circular arcs in Figs. 6 and 7.

From the results in Table 3, the primary backbone is subject to negligible force ($f_p^{(1)} = 0.000 < 10^{-7}N$). According to the Bernoulli–Euler beam theory, a beam with a pure-moment load will resemble a purely circular arc. The obtained loading condition that converges to a pure-moment scenario suggests that the primary backbone bends into a perfectly circular shape.

With results obtained for the distal (first) subsegment, the shape of the remaining subsegments (from the second subsegment to the $n$th subsegment) now can be obtained sequentially by solving $[(\mathbf{x}_a^{(t)})^T\ \alpha^{(t)}]^T$ for the $t$th subsegment from the following nonlinear equations:

**Table 2 Integration results using elliptic integrals**

| $0<\varphi_j^{(t)}<\alpha^{(t)}+\varphi_j^{(t)}\le\pi$ | $0<\varphi_j^{(t)}\le\pi<\alpha^{(t)}+\varphi_j^{(t)}$ |
|---|---|
| $\mathrm{I}_{1j}^{(t)}=\mathrm{I}_{1+}(\pi-\varphi_j^{(t)},a_j^{(t)},f_j^{(t)})-\mathrm{I}_{1+}(\pi-\alpha^{(t)}-\varphi_j^{(t)},a_j^{(t)},f_j^{(t)})$ | $\mathrm{I}_{1j}^{(t)}=\mathrm{I}_{1+}(\alpha^{(t)}+\varphi_j^{(t)}-\pi,a_j^{(t)},f_j^{(t)})+\mathrm{I}_{1+}(\pi-\varphi_j^{(t)},a_j^{(t)},f_j^{(t)})$ |
| $\mathrm{I}_{cj}^{(t)}=\mathrm{I}_{c+}(\pi-\alpha^{(t)}-\varphi_j^{(t)},a_j^{(t)},f_j^{(t)})-\mathrm{I}_{c+}(\pi-\varphi_j^{(t)},a_j^{(t)},f_j^{(t)})$ | $\mathrm{I}_{cj}^{(t)}=-\mathrm{I}_{c+}(\alpha^{(t)}+\varphi_j^{(t)}-\pi,a_j^{(t)},f_j^{(t)})-\mathrm{I}_{c+}(\pi-\varphi_j^{(t)},a_j^{(t)},f_j^{(t)})$ |
| $\varphi_j^{(t)}\le 0<\alpha^{(t)}+\varphi_j^{(t)}\le\pi$ | $-\pi\le\varphi_j^{(t)}<\alpha^{(t)}+\varphi_j^{(t)}<0$ |
| $\mathrm{I}_{1j}^{(t)}=\mathrm{I}_{1-}(\alpha^{(t)}+\varphi_j^{(t)},a_j^{(t)},f_j^{(t)})+\mathrm{I}_{1-}(-\varphi_j^{(t)},a_j^{(t)},f_j^{(t)})$ | $\mathrm{I}_{1j}^{(t)}=\mathrm{I}_{1+}(\alpha^{(t)}+\varphi_j^{(t)}+\pi,a_j^{(t)},f_j^{(t)})-\mathrm{I}_{1+}(\pi+\varphi_j^{(t)},a_j^{(t)},f_j^{(t)})$ |
| $\mathrm{I}_{cj}^{(t)}=\mathrm{I}_{c-}(\alpha^{(t)}+\varphi_j^{(t)},a_j^{(t)},f_j^{(t)})+\mathrm{I}_{c-}(-\varphi_j^{(t)},a_j^{(t)},f_j^{(t)})$ | $\mathrm{I}_{cj}^{(t)}=\mathrm{I}_{c+}(\pi+\varphi_j^{(t)},a_j^{(t)},f_j^{(t)})-\mathrm{I}_{c+}(\pi+\alpha^{(t)}+\varphi_j^{(t)},a_j^{(t)},f_j^{(t)})$ |

$$k_a=\sqrt{\frac{2p}{a+p}} \qquad k_p=\sqrt{\frac{a+p}{2p}} \qquad \gamma_{za+}=\frac{z}{2} \qquad \gamma_{zp+}=\arcsin\sqrt{\frac{p(1-\cos z)}{a+p}} \qquad \gamma_{za-}=\arcsin\sqrt{\frac{(a+p)(1-\cos z)}{2(a-p\cos z)}}$$

$$\mathrm{I}_{1+}(z,a,p)=\begin{cases}\displaystyle\int_0^z\frac{d\vartheta}{\sqrt{a+p\cos\vartheta}}=\frac{2}{\sqrt{a+p}}F(\gamma_{za+},k_a) & (a>p)\\ \displaystyle\int_0^z\frac{d\vartheta}{\sqrt{a+p\cos\vartheta}}=\sqrt{\frac{2}{p}}F(\gamma_{zp+},k_p) & (p>|a|)\end{cases} \tag{25}$$

$$\mathrm{I}_{c+}(z,a,p)=\begin{cases}\displaystyle\int_0^z\frac{\cos\vartheta d\vartheta}{\sqrt{a+p\cos\vartheta}}=\frac{2\sqrt{a+p}}{p}E(\gamma_{za+},k_a)-\frac{2a}{p\sqrt{a+p}}F(\gamma_{za+},k_a) & (a>p)\\ \displaystyle\int_0^z\frac{\cos\vartheta d\vartheta}{\sqrt{a+p\cos\vartheta}}=\sqrt{\frac{2}{p}}(2E(\gamma_{zp+},k_p)-F(\gamma_{zp+},k_p)) & (p>|a|)\end{cases} \tag{26}$$

$$\mathrm{I}_{1-}(z,a,p)=\int_0^z\frac{d\vartheta}{\sqrt{a-p\cos\vartheta}}=\frac{2}{\sqrt{a+p}}F(\gamma_{za-},k_a) \tag{27}$$

$$\mathrm{I}_{c-}(z,a,p)=\int_0^z\frac{\cos\vartheta d\vartheta}{\sqrt{a-p\cos\vartheta}}=\frac{2a}{p\sqrt{a+p}}F(\gamma_{za-},k_a)-\frac{2\sqrt{a+p}}{p}E(\gamma_{za-},k_a)+\frac{2\sin z}{\sqrt{a-p\cos z}} \tag{28}$$

$$\begin{bmatrix}\mathbf{c}_s^{(t)}\\ \mathbf{c}_c^{(t)}\\ \sqrt{E_pI_p/2\mathrm{I}_{1p}^{(t)}-L_{sp}^{(t)}}\end{bmatrix}=\mathbf{0} \tag{29}$$

where $\mathbf{x}_a^{(t)}$ is defined in Eq. (23) ($t=2,3,\ldots,n$) and $\mathbf{c}_s^{(t)}$ and $\mathbf{c}_c^{(t)}$ are defined in Eqs. (2) and (12), respectively.

For a robot with the same subsegment length (identical $L_{sp}^{(t)}$ for all the subsegments), results for the $t$th subsegment ($t=2,3,\ldots,n$) solved from Eq. (29) are identical to the results of the distal (first) subsegment

$$\mathbf{x}_a^{(t)}=\mathbf{x}_a^{(1)}, \quad t=2,3,\ldots,n \tag{30}$$

Then the following relations hold:

**Table 3 Results for the actuation mode 1**

| Unit: N | Unit: rad | Unit: mN m | Unit: mm |
|---|---|---|---|
| $f_1^{(1)}=12.144$ | $\varphi_1^{(1)}=-0.2618$ | $m_1^{(1)}=-28.888$ | $L_{s1}^{(1)}=28.396$ |
| $f_2^{(1)}=8.890$ | $\varphi_2^{(1)}=2.8798$ | $m_2^{(1)}=-0.009$ | $L_{s2}^{(1)}=31.291$ |
| $f_3^{(1)}=3.254$ | $\varphi_3^{(1)}=2.8798$ | $m_3^{(1)}=-10.483$ | $L_{s3}^{(1)}=30.452$ |
| $f_p^{(1)}=0.000$ | $\varphi_p^{(1)}=0.000$ | $m_p^{(1)}=-15.269$ | $L_{sp}^{(1)}=30.000$ |

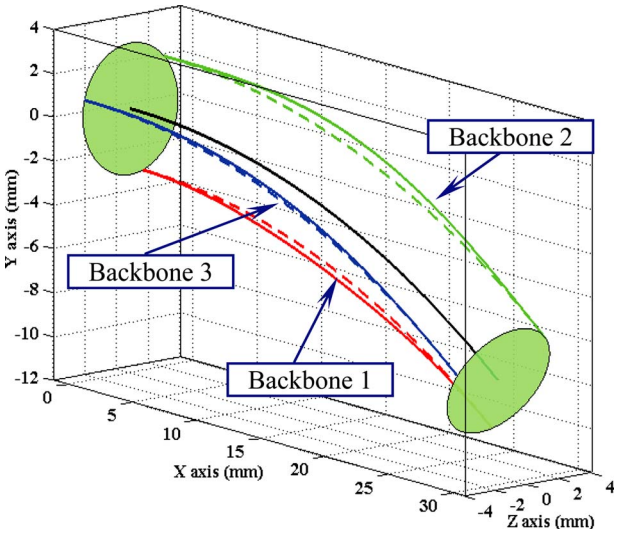


**Fig. 6 The actual shape and circular arcs of one subsegment in actuation mode 1**

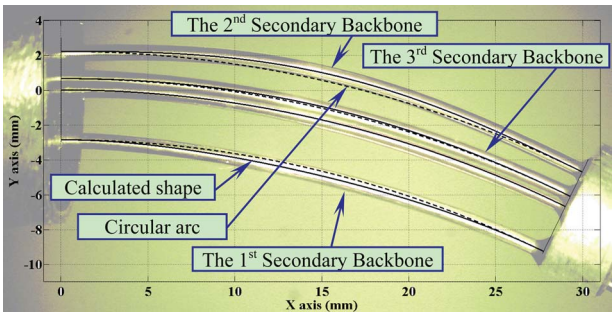


**Fig. 7 The calculated shape (solid lines) and circular arc (dashed lines) overlaid over the actual shape of one subsegment in actuation mode 1**

$$L_i = nL_{si}^{(1)} \tag{31}$$

$$\theta_0 - \theta_L = n\alpha^{(1)} \tag{32}$$

$$q_i = L_i - L = nL_{si}^{(1)} - L \tag{33}$$

$$\tau_i = \mathbf{f}_i^{(n)} \cdot \hat{\mathbf{x}}_s^{(n)}, \quad i = 1,2,3 \tag{34}$$

where $\theta_L$, $q_i$, $\tau_i$, and so on, are defined in the Nomenclature.

This phenomenon can be qualitatively verified according to Fig. 4: If the length of two adjacent subsegments is identical, the $i$th subsegment and the $(i-1)$th subsegment are symmetric with respect to the $XY$ plane of $\{\hat{\mathbf{x}}_s^{(t-1)}, \hat{\mathbf{y}}_s^{(t-1)}, \hat{\mathbf{z}}_s^{(t-1)}\}$ in the absence of external disturbances. Hence, the values of $\mathbf{x}_a^{(t)}$ for these two subsegments should be the same. This symmetry also validates the assumption that spacer disks are perpendicular to the secondary backbones. If the tangent to the secondary backbones is not perpendicular to the spacer disk, this symmetry cannot hold.

The shapes for all of the backbones for the entire robot are now solved. The obtained results validate the assumption of planar bending patterns in Sec. 3.

Please note that in this actuation mode the shape of the primary backbone is exactly circular. A closed-form instantaneous direct kinematics from the configuration space $\boldsymbol{\Psi}$ to the task space $\mathbf{x}$ can be derived, as in Ref. [37]

$$\mathbf{J}_{\mathbf{x}\boldsymbol{\Psi}} = \begin{bmatrix} L\cos\delta\dfrac{(\theta_L-\theta_0)\cos\theta_L - \sin\theta_L + 1}{(\theta_L-\theta_0)^2} & -L\dfrac{\sin\delta(\sin\theta_L - 1)}{\theta_L-\theta_0} \\ -L\sin\delta\dfrac{(\theta_L-\theta_0)\cos\theta_L - \sin\theta_L + 1}{(\theta_L-\theta_0)^2} & -L\dfrac{\cos\delta(\sin\theta_L - 1)}{\theta_L-\theta_0} \\ L\dfrac{(\theta_L-\theta_0)\sin\theta_L + \cos\theta_L}{(\theta_L-\theta_0)^2} & 0 \\ -\sin\delta & \cos\delta\cos\theta_L \\ -\cos\delta & -\sin\delta\cos\theta_L \\ 0 & -1+\sin\theta_L \end{bmatrix} \tag{35}$$

**Table 4 Results for the actuation mode 2**

| Unit: N | Unit: rad | Unit: mN m | Unit: mm |
|---|---|---|---|
| $f_1^{(1)}=13.016$ | $\varphi_1^{(1)}=-0.2618$ | $m_1^{(1)}=-29.680$ | $L_{s1}^{(1)}=28.361$ |
| $f_2^{(1)}=8.120$ | $\varphi_2^{(1)}=2.8798$ | $m_2^{(1)}=-1.595$ | $L_{s2}^{(1)}=31.236$ |
| $f_3^{(1)}=2.456$ | $\varphi_3^{(1)}=2.8798$ | $m_3^{(1)}=-11.681$ | $L_{s3}^{(1)}=30.408$ |
| $f_p^{(1)}=2.440$ | $\varphi_p^{(1)}=2.8798$ | $m_p^{(1)}=-11.958$ | $L_{sp}^{(1)}=30.000$ |

The exact inverse kinematics from the configuration space $\boldsymbol{\Psi}$ to the joint space $\mathbf{q}$ is shown in Eq. (33). However, there is not a closed-form expression for $\mathbf{J}_{\mathbf{q}\boldsymbol{\Psi}}$.

*Actuation mode 2*. Distributed loads on all the backbones. It was shown in Ref. [38] that the use of multiple flexible backbones could allow improved distribution of load among the backbones via proper actuation redundancy resolutions. This property will be explored here. One possible formulation of this load redistribution problem could be the same as the minimization problem in Eq. (23) for $\mathbf{f}_{\text{user}}=[5\ 5\ 5\ 5]^T$ and $\mathbf{W}=\text{diag}(1/(E_sI_s),\ 1/(E_sI_s),\ 1/(E_sI_s),\ 1/(E_pI_p))$. Larger values in $\mathbf{f}_{\text{user}}$ lead to smaller compressive forces, since the compressive forces are defined negative in $\{\hat{\mathbf{x}}_s^{(t)}, \hat{\mathbf{y}}_s^{(t)}, \hat{\mathbf{z}}_s^{(t)}\}$. However, values in $\mathbf{f}_{\text{user}}$ should not be too large otherwise the pulling force on one backbone can exceed the strength of the backbone or the strength of the backbone-to-end-disk connection. $\mathbf{W}$ takes the bending stiffness of each backbone into account.

Simulation results are listed in Table 4 as well as plotted in Fig. 8 for the same structure defined by Table 1. Figure 8 also draws the shape of the subsegment under actuation mode 1.

As shown in Fig. 8(*a*), the end disk is retracted in the $\hat{\mathbf{x}}_s^{(1)}$ direction with the orientation remaining the same in actuation mode 2. The end disk retraction is about 0.03 mm or 0.01% of the subsegment length.

The rest of the subsegments can be solved using Eq. (29) to form the kinematics for actuation mode 2.

From the obtained results, the structural characteristics of this type of continuum robot can be concluded: loads on the backbones can be redistributed by fine actuation of the secondary backbones. The position variation in the tip is truly negligible and the orientation will remain the same.

In this actuation mode, although the exact shape can be obtained, neither the instantaneous inverse kinematics nor the instantaneous direct kinematics has a closed-form expression. Although load distributions for the two actuation modes are very different, the shape discrepancy between them is quite small. An approximate model is derived and validated through experiments in Sec. 4.2.

Results in Tables 3 and 4 can be qualitatively justified through Fig. 9, which shows the distal subsegment subject to no external disturbance. Since the constraint conditions at the two disks in Fig. 9 are symmetric (at both disks, backbones are perpendicular to the disks and all are in static equilibrium), there should be a central plane, to which the shape and loading conditions of the backbones are symmetric. The forces exerted on the backbones by the robot disk $G_1^{(1)}G_2^{(1)}G_3^{(1)}$ would only have components in the

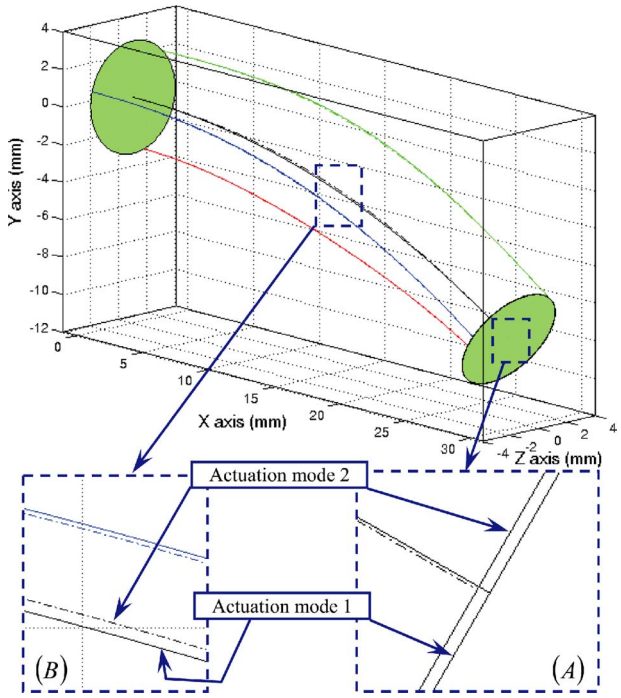


**Fig. 8 Calculated shapes of the last subsegment under different actuation modes: insets (*a*) and (*b*) provide enlarged side views**

direction of $\hat{\mathbf{x}}_c$. If there were $Y$ components in these forces, the other robot disk in Fig. 9 would generate identical $Y$ components due to the symmetry. Since there is no external force to balance them, the $Y$ component cannot exist. Hence, all of the forces will be in the direction of $\hat{\mathbf{x}}_c$ or $-\hat{\mathbf{x}}_c$, as seen in Tables 3 and 4, where $\varphi_j^{(1)}$ values are either identical or offset by $\pi$. Furthermore, $m_2^{(1)}$ values in Tables 3 and 4 are small, which indicates the bending shape of the next secondary backbone, which is generated mainly by the compressing force $\mathbf{f}_2^{(1)}$.

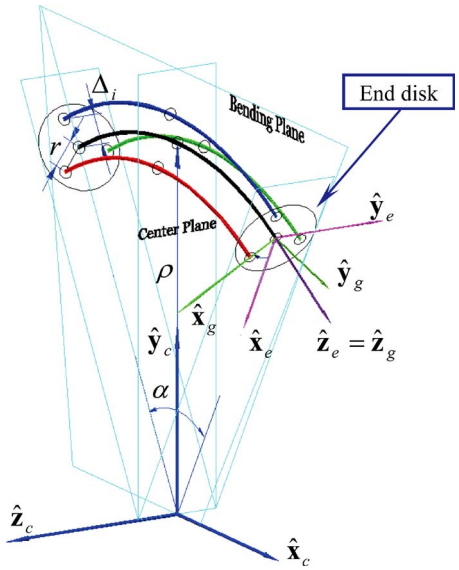


**Fig. 9 Diagram for qualitative justification of the simulation results**

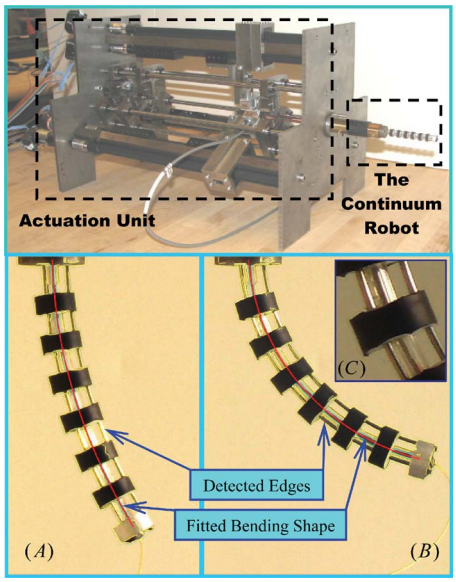


**Fig. 10 A Ø7.5 mm continuum robot with its actual bending shape under configurations of (*a*) $\theta_L$=60 deg, $\delta$=0 deg; (*b*) $\theta_L$=15 deg, $\delta$=0 deg, and (*c*) a close-up view of one spacer disk**

**4.2 An Approximate Kinematic Model and Its Experimental Validation.** When these continuum robots are implemented as distal dexterity enablers, a formulation of the inverse kinematics from the configuration space $\mathbf{\Psi}$ to the joint space $\mathbf{q}$ for fast calculation is required to facilitate telemanipulation and the robot control [6,39]. Based on the fact proved in Sec. 4.1 that the shape of the continuum robot is circular under the actuation mode 1, an approximate formulation of the inverse kinematics is derived, also available in Refs. [11,22,24]

$$L_i = L + q_i = L + \Delta_i(\theta_L - \theta_0) \tag{36}$$

$$\Delta_i \equiv r\cos(\delta_i), \quad i = 1,2,3 \tag{37}$$

This approximate model is verified by a continuum robot and its actuation unit, as shown in Figs. 10(*a*)–10(*c*). The diameter of this robot is 7.5 mm. Each secondary backbone is actuated in a push-pull mode by the actuation unit. The linear slider and the encoder at the motor shafts allow a positioning accuracy of 0.025 mm.

The robot was actuated by rods, which were glued to the secondary backbones. These actuation rods were driven by lead screws in the actuation unit. Actuation length $q_i$ is calculated using the approximate model, Eq. (36). A series of pictures of the robot shown in Figs. 10(*a*)–10(*c*) was taken while the robot was bent to different angles. These pictures were transformed into gray scale and edges were detected using Canny masks [40]. Then a third order polynomial was fitted to each bending shape of the robot to parameterize the shape [37].

Figure 11 shows the actual shape of the primary backbone compared with a circular shape, when the actual end effector angle is set equal to: $\theta_L$=70 deg, $\theta_L$=40 deg, and $\theta_L$=15 deg. To quantitatively estimate how close the actual bending shape is to a circular shape, the actual tip position is calculated by an integral along the actual primary backbone shape. The results show that the robot tip position variation is smaller than $\pm$0.45 mm.

When actuation commands were issued according to Eq. (36), the actual $\theta_L$ was larger than the desired value (less bending). A series of experiments were conducted. The actual $\theta_L$ was extracted from pictures similar to the ones shown in Figs. 10(*a*)–10(*c*). The actual versus the desired values of $\theta_L$ were plotted in Fig. 12. A linear regression was fitted to these experimental results and the result is given in Eq. (38), where $\bar{\theta}_L$ is the desired end effector value, $\kappa$=1.169 and $\theta_{Lc}$=15.21 deg.

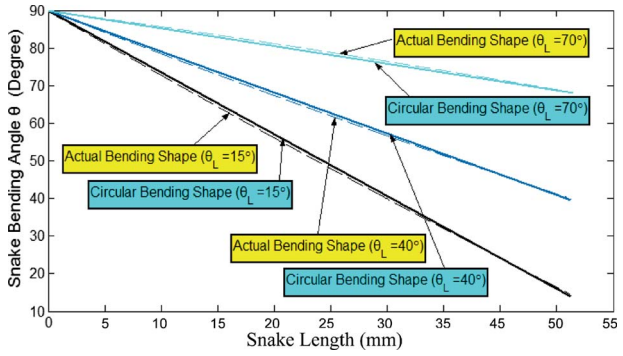


**Fig. 11 Bending shape along the primary backbone of the continuum robot**

$$\bar{\theta}_L = \kappa\theta_L - \theta_{Lc} \tag{38}$$

The appearance of $\theta_{Lc}$ is due to defining the straight configuration as $\theta_L = \pi/2$. Based on the experimental results, Eq. (36) needs to be corrected as follows:

$$L_i = L + q_i = L + \Delta_i((\kappa\theta_L - \theta_c) - \theta_0) \tag{39}$$

Equation (36) is from the approximate kinematic model based on the assumption that all of the backbones are circular. Equation (39) is from Eq. (36) based on experimental corrections. In order to compare the theoretic results with the experimental results, theoretic results of $\mathbf{q}$ solved from Sec. 4.1 are plotted in Fig. 13, together with $\mathbf{q}$ values calculated from Eq. (39). From Fig. 13, there is still some discrepancy between the theoretical results and the experimental results. This can be due to the manufacturing and assembling accuracy, compliance of the actuation unit, material uncertainties, local bending within the holes in the spacer disks, system friction, and so on.

## 5 Shape Restoration

When an external wrench is exerted at the tip of the continuum robot, the structure is deformed, which involves variations in both the tip orientation and the tip position. The deflection can be quantified and the robot can be actuated to partially restore its original shape.

The external force $\mathbf{f}_e$ and moment $\mathbf{m}_e$ can be precisely estimated according to Ref. [37]. However, they are expressed in $\{\hat{\mathbf{x}}_b, \hat{\mathbf{y}}_b, \hat{\mathbf{z}}_b\}$ instead of in $\{\hat{\mathbf{x}}_s^{(1)}, \hat{\mathbf{y}}_s^{(1)}, \hat{\mathbf{z}}_s^{(1)}\}$. Before they can be substituted into Eq. (1), they need to be transformed into $\{\hat{\mathbf{x}}_s^{(1)}, \hat{\mathbf{y}}_s^{(1)}, \hat{\mathbf{z}}_s^{(1)}\}$. This transformation is unknown because with $\mathbf{f}_e$ and $\mathbf{m}_e$ applied,

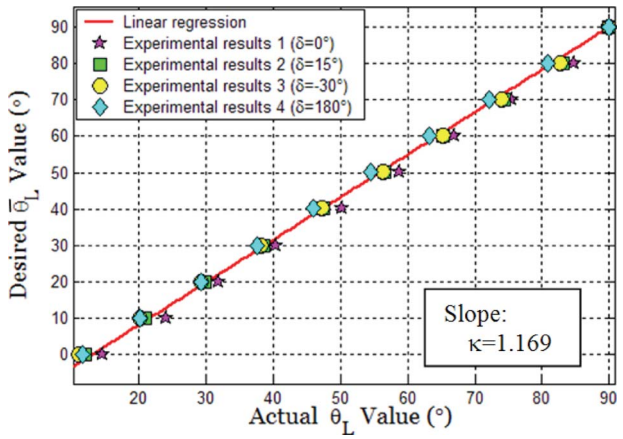


**Fig. 12 Actual $\theta_L$ value versus desired $\bar{\theta}_L$ value**

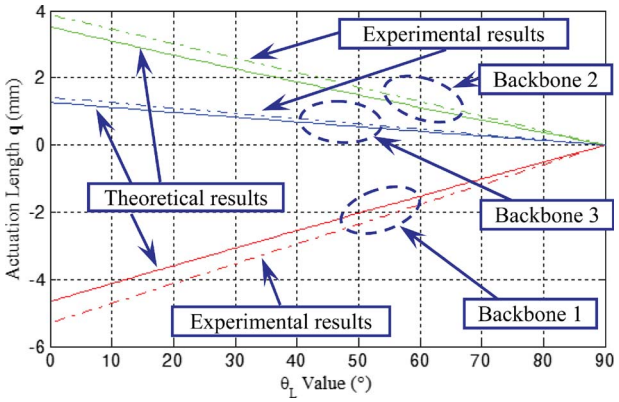


**Fig. 13 The theoretical results from Sec. 4.1 compared with the experimentally corrected results in the joint space**

all the $\alpha^{(t)}$ $(t=1,2,3,\ldots,n)$ could be changed. Hence, calculation of both the shape restoration and the deflection will involve a shooting method.

The shooting method starts with the actual shape of the robot before the external loads $\mathbf{f}_e$ and $\mathbf{m}_e$ are applied. The steps include the following. Some entities are also indicated in Fig. 14 for a clearer explanation.

- Initial values of $\alpha^{(t)}$ $(t=1,2,3,\ldots,n)$ are used to calculate the transformation from $\{\hat{\mathbf{x}}_b, \hat{\mathbf{y}}_b, \hat{\mathbf{z}}_b\}$ to $\{\hat{\mathbf{x}}_s^{(1)}, \hat{\mathbf{y}}_s^{(1)}, \hat{\mathbf{z}}_s^{(1)}\}$.
- The transformed $\mathbf{f}_e$ and $\mathbf{m}_e$ are now substituted into Eq. (1) to form the constraint of $\mathbf{c}_s^{(1)}$.
- A new value of $\alpha^{(1)}$ (designated by $\tilde{\alpha}^{(1)}$) is assumed. With predefined $\mathbf{f}_{\text{user}}$ and $\mathbf{W}$, Eq. (23) is solved.
- The remaining subsegments are solved sequentially using Eq. (29), updated values of $\alpha^{(t)}$ (designated by $\tilde{\alpha}^{(t)}$) $(t=2,3,\ldots,n)$ are obtained.
- $\tilde{\alpha}^{(1)}$ is adjusted until the shooting target is reached.

The shooting targets for the computations of the deflection, the tip position restoration, and the tip orientation restoration are all different.

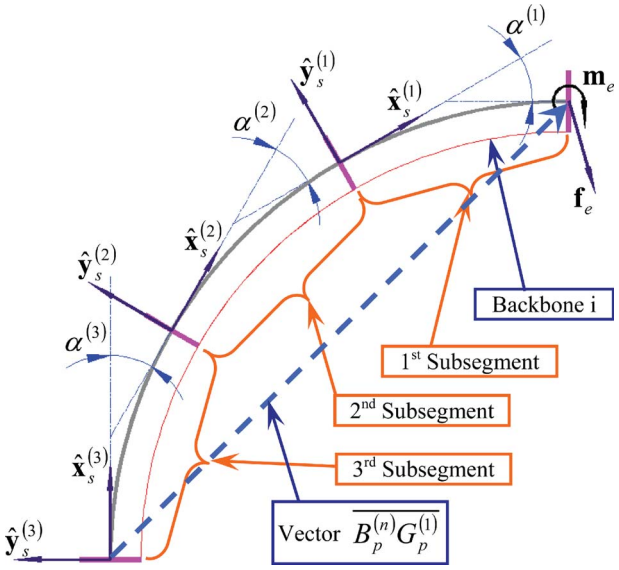


**Fig. 14 The shooting method is initialized using the local tangents of the subsegments based on the shape of an unloaded robot**

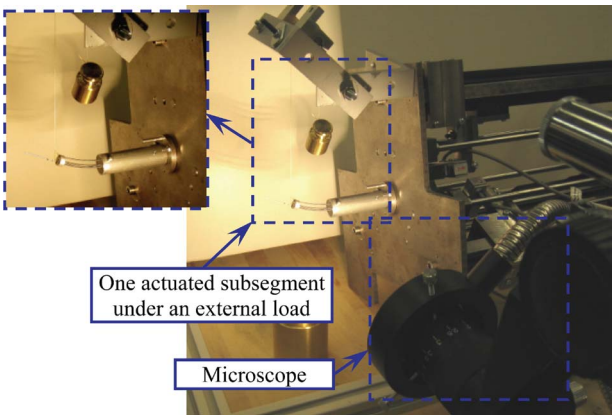


**Fig. 15 Experimental setup for validating shape restoration**

For the restoration of the tip orientation, the shoot target is simply the following, which states that the overall bending angle remains the same:

$$\theta_0 - \theta_L = \sum_{t=1}^{n} \alpha^{(t)} \tag{40}$$

For the restoration of the tip position, the shooting target is formulated as follows:

$${}^{b}\overline{B_p^{(n)} G_p^{(1)}} = {}^{b}(\overline{B_p^{(n)} G_p^{(1)}})_{\text{no load}} \tag{41}$$

This target states the position vector from $B_p^{(n)}$ to $G_p^{(1)}$ in $\{\hat{\mathbf{x}}_b, \hat{\mathbf{y}}_b, \hat{\mathbf{z}}_b\}$ remains the same.

For the calculation of the robot's deflected shape under the external wrench, the shooting target is as shown below, which indicates that the length of the $i$th secondary backbone remains the same before and after the external load is applied

$$\sum_{t=1}^{n} L_{si}^{(t)} = \left( \sum_{t=1}^{n} L_{si}^{(t)} \right)_{\text{no load}}, \quad i = 1,2,3 \tag{42}$$

As the aforementioned procedures show, calculations of the shape deflection or of the shape restoration are independent processes. Hence, shape restoration can be obtained without calculating the deflected shape.

For demonstration purposes, a one-subsegment robot is actuated and then deformed. The restorations of its tip orientation and its tip position are simulated.

As shown in Fig. 15, the subsegment is bent to 30 deg and then an external force of $\mathbf{f}_e = [0 \; -0.5 \; 0]^T$ in $\{\hat{\mathbf{x}}_s^{(1)}, \hat{\mathbf{y}}_s^{(1)}, \hat{\mathbf{z}}_s^{(1)}\}$ was applied. Numerical values for the parameters are listed in Table 1. Please note that the subsegment is bending upwards in Fig. 15 because the image from the utilized microscope is flipped. By bending upwards, the experimental results and the simulation are kept consistent.

Table 5 lists all of the calculation results, where $T_{px}$ and $T_{py}$ are

**Table 5 Results for the shape restoration**

| No load | Deflected | Orientation restored | Position restored |
|---|---|---|---|
| $\alpha^{(1)}=30$ deg | $\alpha^{(1)}=30.23$ deg | $\alpha^{(1)}=30$ deg | $\alpha^{(1)}=28.81$ deg |
| $T_{px}=28.618$ | $T_{px}=28.524$ | $T_{px}=28.539$ | $T_{px}=28.619$ |
| $T_{py}=-7.668$ | $T_{py}=-8.013$ | $T_{py}=-7.955$ | $T_{py}=-7.668$ |
| $L_{s1}^{(1)}=28.361$ | $L_{s1}^{(1)}=28.361$ | $L_{s1}^{(1)}=28.367$ | $L_{s1}^{(1)}=28.438$ |
| $L_{s2}^{(1)}=31.236$ | $L_{s2}^{(1)}=31.236$ | $L_{s2}^{(1)}=31.209$ | $L_{s2}^{(1)}=31.150$ |
| $L_{s3}^{(1)}=30.408$ | $L_{s3}^{(1)}=30.408$ | $L_{s3}^{(1)}=30.402$ | $L_{s3}^{(1)}=30.385$ |
| $L_{sp}^{(1)}=30.000$ | $L_{sp}^{(1)}=30.000$ | $L_{sp}^{(1)}=30.000$ | $L_{sp}^{(1)}=30.000$ |

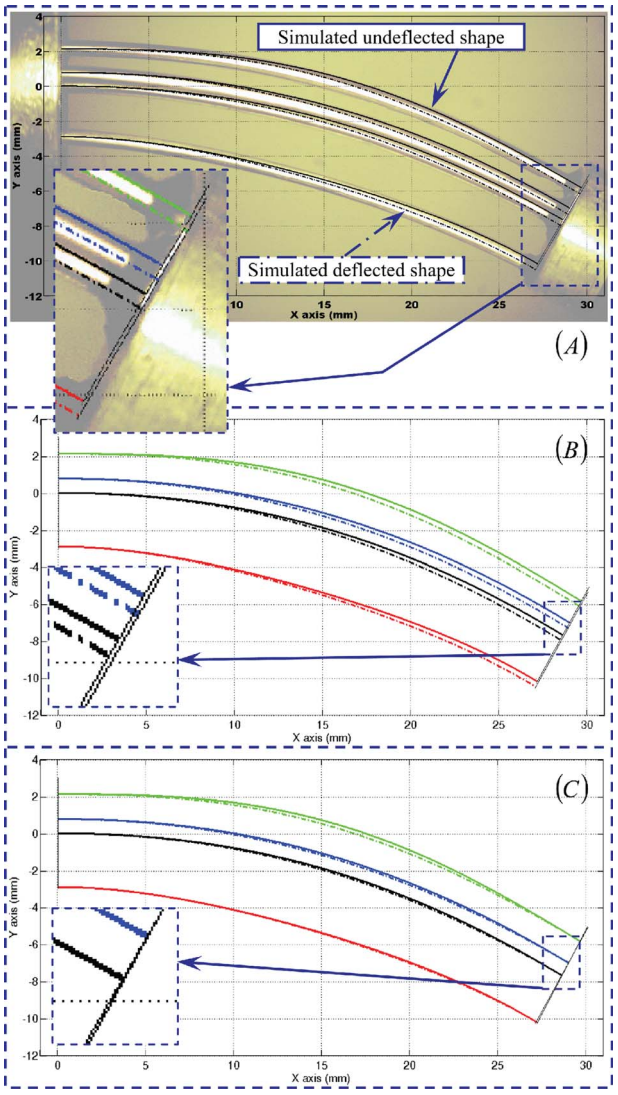


**Fig. 16 Shape restoration simulation and experiment: (*a*) simulated deflected and simulated undeflected shapes overlaid over an actual externally loaded subsegment, (*b*) simulation of the deflected subsegment in (*a*) with and without tip orientation restoration, and (*c*) simulation of the deflected subsegment in (*a*) with and without tip position restoration**

the $XY$ coordinates of the tip position of the primary backbone. The units in Table 5 are all millimeters, except in the first row. Comparing the first and the second column in Table 5 and referring to Fig. 16(*a*), when $\mathbf{f}_e$ is applied, the subsegment is deflected downwards with $\alpha^{(1)}$ increased, while $L_{si}^{(1)}$ remains the same. In Figs. 16(*a*)–16(*c*), the actual defected shape fits the calculation results well; the maximal discrepancy between the actual deflected shape and the predicted result is 0.15 mm.

Figure 16(*b*) plots the shape with the tip orientation restored, while Fig. 16(*c*) plots the shape with the tip position restored. The calculation results are listed in the third and fourth column in Table 5. Actuating the secondary backbones to these new $L_{si}^{(1)}$ values will partially restore the robot's shape. All of the results in Figs. 16(*a*)–16(*c*) and Table 5 were generated under the actuation mode 2 (mentioned in Sec. 4.1).

We note that shape can only be partially restored because of parasitic motions/deflections resulting from external disturbances. One may define control strategies for compensating for these deflections. For example, Ref. [41] considered a recursive linear estimation approach that uses external monitoring of the end disk

orientation in order to overcome parasitic motions that stem from the flexibility of the actuation lines. The same approach may be considered for compliant parasitic motions. In a realistic surgical scenario, these robots are telemanipulated by a surgeon who has full view of the surgical field. The user inherently compensates for the parasitic motions. Results of the preliminary telemanipulation study using this robot were reported in Ref. [42].

## 6 Conclusion

This paper presented an analytic formulation for kinematics, statics, and shape restoration of a new type of continuum robot with multiple flexible backbones. Although a comprehensive study should also include an analysis of the structural stability (backbone buckling), with enormous results directly applicable from previous studies (e.g., Ref. [43] and example No. 1 from Ref. [44]), this paper chose to focus on deriving the kinestatic and stiffness properties of the robot via an analytic approach, which uses elliptic integrals.

Two major problems were studied in this paper. The actuation redundancy resolution problem of the continuum robots was first solved. It was shown that the shape of the entire robot is perfectly circular when applying one particular actuation redundancy resolution. This provided a proof to the experimentally verified assumption that this type of continuum robot bends into a circular shape, which was used in the authors' previous studies. In addition, a closed-form direct kinematics from the configuration space $\boldsymbol{\Psi}$ to the task space $\mathbf{x}$ was also obtained. The other actuation resolution was also solved, showing that the loads on all of the backbones can be redistributed without introducing significant variation on the robot's shape. This property reduces the risk of backbone buckling and supports further miniaturization of this robot. Based on these solutions, an approximate model was derived and experimentally validated.

The shape restoration problem was solved and the derived actuation strategies were shown to achieve a partial shape restoration of the robot. Although the deflection could be also quantified through a shooting method, a formulation of this shape restoration problem provided an additional advantage that the shape restoration could now be obtained without calculating the actual deflection. The implementation of this shape restoration algorithm in a real-time environment is being considered.


## Acknowledgment

This is supported by NSF Career Award No. 0844969 and by Columbia University internal funds.


## Nomenclature

- $i$ = index of the secondary backbones, $i=1,2,3$
- $j$ = index of all the backbones, $j=1,2,3,p$
- $n$ = number of the subsegments in the continuum robot
- $L, L_i$ = length of the primary and the $i$th secondary backbone measured from the base disk to the end disk
- $L_{sp}^{(t)}, L_{si}^{(t)}$ = length of the primary and the $i$th secondary backbone within the $t$th subsegment, $L_i=\Sigma_{t=1}^{n} L_{si}^{(t)}$ and $L=\Sigma_{t=1}^{n} L_{sp}^{(t)}$
- $\mathbf{q}$ = $\mathbf{q}=[q_1 \ q_2 \ q_3]^T$ is the actuation lengths of the secondary backbones and $q_i=L_i-L$
- $r$ = radius of the pitch circle defining the positions of the secondary backbones in all the disks
- $\beta$ = division angle of the secondary backbones along the circumference of the pitch circle, $\beta=2\pi/3$
- $\rho(s)$ = radius of curvature of the primary backbone
- $\rho_i(s)$ = radius of curvature of the $i$th secondary backbone
- $\theta(s)$ = the angle between $\hat{\mathbf{z}}_1$ and the tangent to the primary backbone in the bending plane; $\theta(L)$ and $\theta(0)$ are designated by $\theta_L$ and $\theta_0$, respectively; $\theta_0=\pi/2$
- $\delta_i$ = a right-handed rotation angle about $\hat{\mathbf{z}}_1$ from $\hat{\mathbf{x}}_1$ to a line passing through the primary backbone and the $i$th secondary backbone at $s=0$; at a straight configuration, $\hat{\mathbf{x}}_1$ is along the same direction as the desired instantaneous linear velocity of the end disk
- $\delta$ = $\delta\equiv\delta_1$ and $\delta_i=\delta+(i-1)\beta$, $i=1,2,3$; in Figs. 2($a$) and 2($b$), $\delta=-\pi/12=-15$ deg
- $\boldsymbol{\Psi}$ = $\boldsymbol{\Psi}\equiv[\theta_L \ \delta]^T$ is a two-dimensional vector that is used to characterize the configuration of the continuum robot
- $\Delta_i$ = radial offset from the primary backbone to the projection of the $i$th secondary backbone on the bending plane
- $\boldsymbol{\tau}$ = $\boldsymbol{\tau}=[\tau_1 \ \tau_2 \ \tau_3]^T$ is the actuation forces of the secondary backbones (positive $\tau_i$ defined as pushing)
- $E_p, E_i$ = Young's modulus of the primary and the $i$th secondary backbone
- $I_p, I_i$ = cross-sectional moments of inertia of the primary and the $i$th secondary backbone
- ${}^1\mathbf{R}_2$ = rotation matrix of frame 2 with respect to frame 1
- $d_{op}, d_{oi}$
- $d_{ip}, d_{ii}$ = outer and inner diameters of the primary and the $i$th secondary backbone, respectively
- $\mathbf{J_{yx}}$ = Jacobian matrix of the mapping $\dot{\mathbf{y}}=\mathbf{J_{yx}}\dot{\mathbf{x}}$ where the dot over the variable represents the time derivative
- $\dot{\mathbf{x}}$ = the twist $\dot{\mathbf{x}}\in\Re^{6\times1}$ of the end disk, defined with the linear velocity preceding the angular velocity
- $B_p^{(t)}, B_i^{(t)}$ = starting points of the primary and the $i$th secondary backbone within the $t$th subsegment
- $G_p^{(t)}, G_i^{(t)}$ = ending points of the primary and the $i$th secondary backbone within the $t$th subsegment
- $\theta_{L_{sj}^{(t)}}$ = the angle between $\hat{\mathbf{x}}_s^{(t)}$ and the tangent to the backbone at $G_j^{(t)}$ point in $\{\hat{\mathbf{x}}_s^{(t)}, \hat{\mathbf{y}}_s^{(t)}, \hat{\mathbf{z}}_s^{(t)}\}$
- $\alpha^{(t)}$ = bending angle of the $t$th ($t=1,2,\ldots,n$) subsegment, shown in Fig. 2($c$). its value is assumed to be positive
- $\mathbf{f}_p^{(t)}, \mathbf{f}_i^{(t)}$ and $\mathbf{m}_p^{(t)}, \mathbf{m}_i^{(t)}$ = forces and moments acting at the tip of the primary and the $i$th secondary backbone by the robot disks, in the $t$th subsegment

## Appendix A

Equation (11) can be rearranged as the following:

$$(\overline{B_p^{(t)}G_p^{(t)}} - \overline{B_i^{(t)}G_i^{(t)}})|_{x,y} = (\overline{B_p^{(t)}B_i^{(t)}} - \overline{G_p^{(t)}G_i^{(t)}})|_{x,y} \tag{A1}$$

Vectors $\overline{B_p^{(t)}B_i^{(t)}}$ and $\overline{G_p^{(t)}G_i^{(t)}}$ are expressed in $\{\hat{\mathbf{x}}_s^{(t)}, \hat{\mathbf{y}}_s^{(t)}, \hat{\mathbf{z}}_s^{(t)}\}$ as the following:

$$\overline{B_p^{(t)}B_i^{(t)}} = -r\begin{bmatrix}0 & \cos\delta_i & \sin\delta_i\end{bmatrix}^T \tag{A2}$$

$$\overline{G_p^{(t)}G_i^{(t)}} = -r\begin{bmatrix}\sin\alpha^{(t)}\cos\delta_i & \cos\alpha^{(t)}\cos\delta_i & \sin\delta_i\end{bmatrix}^T \tag{A3}$$

The right hand side of Eq. (A1) becomes

$$\overline{B_p^{(t)}B_i^{(t)}} - \overline{G_p^{(t)}G_i^{(t)}} = \begin{bmatrix} r\sin\alpha^{(t)}\cos\delta_i \\ r\cos\delta_i(\cos\alpha^{(t)}-1) \\ 0 \end{bmatrix} \tag{A4}$$

From Eqs. (8) and (9)

$$(\overline{B_p^{(t)}G_p^{(t)}} - \overline{B_i^{(t)}G_i^{(t)}})|_x = \sqrt{\frac{E_pI_p}{2}}\mathrm{Int}_{cp}^{(t)} - \sqrt{\frac{E_iI_i}{2}}\mathrm{Int}_{ci}^{(t)} \tag{A5}$$

$$(\overline{B_p^{(t)}G_p^{(t)}} - \overline{B_i^{(t)}G_i^{(t)}})|_y = \sqrt{\frac{E_pI_p}{2}}\mathrm{Int}_{sp}^{(t)} - \sqrt{\frac{E_iI_i}{2}}\mathrm{Int}_{si}^{(t)} \tag{A6}$$

Combining the above results gives Eq. (12).

## Appendix B

Substituting Eq. (10) into Eqs. (7)–(9)

$$I_{1j}^{(t)} \equiv \int_0^{-\alpha^{(t)}} \frac{-d\theta}{\sqrt{a_j^{(t)} - f_j^{(t)}\cos(\theta-\varphi_j^{(t)})}} \tag{B1}$$

$$\mathrm{Int}_{cj}^{(t)} \equiv \int_0^{-\alpha^{(t)}} \frac{-\cos\theta d\theta}{\sqrt{a_j^{(t)} - f_j^{(t)}\cos(\theta-\varphi_j^{(t)})}} \tag{B2}$$

$$\mathrm{Int}_{sj}^{(t)} \equiv \int_0^{-\alpha^{(t)}} \frac{-\sin\theta d\theta}{\sqrt{a_j^{(t)} - f_j^{(t)}\cos(\theta-\varphi_j^{(t)})}} \tag{B3}$$

After *change* of the variables ($\theta \rightarrow \varphi_j^{(t)} - \theta$), the above integrals simplify as

$$I_{1j}^{(t)} = \int_{\varphi_j^{(t)}}^{\alpha^{(t)}+\varphi_j^{(t)}} \frac{d\theta}{\sqrt{a_j^{(t)} - f_j^{(t)}\cos\theta}} \tag{B4}$$

$$\mathrm{Int}_{cj}^{(t)} = \int_{\varphi_j^{(t)}}^{\alpha^{(t)}+\varphi_j^{(t)}} \frac{\cos\varphi_j^{(t)}\cos\theta + \sin\varphi_j^{(t)}\sin\theta}{\sqrt{a_j^{(t)} - f_j^{(t)}\cos\theta}} d\theta \tag{B5}$$

$$\mathrm{Int}_{sj}^{(t)} = \int_{\varphi_j^{(t)}}^{\alpha^{(t)}+\varphi_j^{(t)}} \frac{\sin\varphi_j^{(t)}\cos\theta - \cos\varphi_j^{(t)}\sin\theta}{\sqrt{a_j^{(t)} - f_j^{(t)}\cos\theta}} d\theta \tag{B6}$$

Hence, the following results are obtained:

$$\mathrm{Int}_{cj}^{(t)} = \cos\varphi_j^{(t)}\mathrm{I}_{cj}^{(t)} + \sin\varphi_j^{(t)}\mathrm{I}_{sj}^{(t)} \tag{B7}$$

$$\mathrm{Int}_{sj}^{(t)} = \sin\varphi_j^{(t)}\mathrm{I}_{cj}^{(t)} - \cos\varphi_j^{(t)}\mathrm{I}_{sj}^{(t)} \tag{B8}$$

$$\mathrm{I}_{cj}^{(t)} = \int_{\varphi_j^{(t)}}^{\alpha^{(t)}+\varphi_j^{(t)}} \frac{\cos\theta d\theta}{\sqrt{a_j^{(t)} - f_j^{(t)}\cos\theta}} \tag{B9}$$

$$\mathrm{I}_{sj}^{(t)} = \int_{\varphi_j^{(t)}}^{\alpha^{(t)}+\varphi_j^{(t)}} \frac{\sin\theta d\theta}{\sqrt{a_j^{(t)} - f_j^{(t)}\cos\theta}} \tag{B10}$$

Equation (B10) can be directly integrated

$$\mathrm{I}_{sj}^{(t)} = \frac{2}{f_j^{(t)}}(\sqrt{a_j^{(t)} - f_j^{(t)}\cos(\alpha^{(t)}+\varphi_j^{(t)})} - \sqrt{a_j^{(t)} - f_j^{(t)}\cos\varphi_j^{(t)}}) \tag{B11}$$

Depending on the range of $\varphi_j^{(t)}$ as listed in Table 2, Eqs. (B4) and (B9) have analytic expressions using the identities of 289.00, 289.03, 293.07, 331.01, 290.00, 290.04, 291.00, 291.03, 315.02, and 318.02 from Ref. [33].

## Appendix C

The term

$$\frac{\partial}{\partial \mathbf{x}_a^{(1)}}\left(\left[(\mathbf{c}_s^{(1)})^T(\mathbf{c}_c^{(1)})^T\sqrt{\frac{E_pI_p}{2}}\mathrm{I}_{1p}^{(1)} - L_{sp}^{(1)}\right]^T\right)$$

involves the partial derivatives of the incomplete elliptic integrals of the first kind and the second kind, which can be derived from their definitions

$$\frac{\partial F}{\partial z} = \frac{1}{\sqrt{1-k^2\sin^2(z)}} \tag{C1}$$

$$\frac{\partial F}{\partial k} = \frac{E(z,k)}{k(1-k^2)} - \frac{F(z,k)}{k} - \frac{k\sin z\cos z}{(1-k^2)\sqrt{1-k^2\sin^2 z}} \tag{C2}$$

$$\frac{\partial E}{\partial z} = \sqrt{1-k^2\sin^2(z)} \tag{C3}$$

$$\frac{\partial E}{\partial k} = \frac{E(z,k)-F(z,k)}{k} \tag{C4}$$

Based on the above results, the following could be obtained to form the derivative matrix:

$$\frac{\partial\,\mathrm{Int}_{cj}^{(1)}}{\partial f_j^{(1)}} = c_{\varphi_j^{(1)}}\frac{\partial \mathrm{I}_{cj}^{(1)}}{\partial f_j^{(1)}} + s_{\varphi_j^{(1)}}\frac{\partial \mathrm{I}_{sj}^{(1)}}{\partial f_j^{(1)}} \tag{C5}$$

$$\frac{\partial\,\mathrm{Int}_{cj}^{(1)}}{\partial \varphi_j^{(1)}} = -s_{\varphi_j^{(1)}}\mathrm{I}_{cj}^{(1)} + c_{\varphi_j^{(1)}}\frac{\partial \mathrm{I}_{cj}^{(1)}}{\partial \varphi_j^{(1)}} + c_{\varphi_j^{(1)}}\mathrm{I}_{sj}^{(1)} + s_{\varphi_j^{(1)}}\frac{\partial \mathrm{I}_{sj}^{(1)}}{\partial \varphi_j^{(1)}} \tag{C6}$$

$$\frac{\partial\,\mathrm{Int}_{cj}^{(1)}}{\partial m_j^{(1)}} = c_{\varphi_j^{(1)}}\frac{\partial \mathrm{I}_{cj}^{(1)}}{\partial m_j^{(1)}} + s_{\varphi_j^{(1)}}\frac{\partial \mathrm{I}_{sj}^{(1)}}{\partial m_j^{(1)}} \tag{C7}$$

$$\frac{\partial\,\mathrm{Int}_{sj}^{(1)}}{\partial f_j^{(1)}} = s_{\varphi_j^{(1)}}\frac{\partial \mathrm{I}_{cj}^{(1)}}{\partial f_j^{(1)}} - c_{\varphi_j^{(1)}}\frac{\partial \mathrm{I}_{sj}^{(1)}}{\partial f_j^{(1)}} \tag{C8}$$

$$\frac{\partial\,\mathrm{Int}_{sj}^{(1)}}{\partial \varphi_j^{(1)}} = c_{\varphi_j^{(1)}}\mathrm{I}_{cj}^{(1)} + s_{\varphi_j^{(1)}}\frac{\partial \mathrm{I}_{cj}^{(1)}}{\partial \varphi_j^{(1)}} + s_{\varphi_j^{(1)}}\mathrm{I}_{sj}^{(1)} - c_{\varphi_j^{(1)}}\frac{\partial \mathrm{I}_{sj}^{(1)}}{\partial \varphi_j^{(1)}} \tag{C9}$$

$$\frac{\partial\,\mathrm{Int}_{sj}^{(1)}}{\partial m_j^{(1)}} = s_{\varphi_j^{(1)}}\frac{\partial \mathrm{I}_{cj}^{(1)}}{\partial m_j^{(1)}} - c_{\varphi_j^{(1)}}\frac{\partial \mathrm{I}_{sj}^{(1)}}{\partial m_j^{(1)}} \tag{C10}$$

The expression for $\mathrm{I}_{cj}^{(1)}$ is available in Table 2 and its partial derivatives also have four different expression sets depending on the value of $\varphi_j^{(1)}$.

## References


[1] Robinson, G., and Davies, J. B., 1999, "Continuum Robots—A State of the Art," IEEE International Conference on Robotics and Automation (ICRA), Detroit, MI, pp. 2849–2853.

[2] Suzumori, K., Iikura, S., and Tanaka, H., 1992, "Applying a Flexible Microactuator to Robotic Mechanisms," IEEE Control Syst. Mag., **12**(1), pp. 21–27.

[3] Suzumori, K., Wakimoto, S., and Takata, M., 2003, "A Miniature Inspection Robot Negotiating Pipes of Widely Varying Diameter," IEEE International Conference on Robotics and Automation (ICRA), Taipei, Taiwan, pp. 2735–2740.

[4] Immega, G., and Antonelli, K., 1995, "The KSI Tentacle Manipulator," IEEE International Conference on Robotics and Automation (ICRA), Nagoya, Aichi, Japan, pp. 3149–3154.

[5] Lane, D. M., Davies, J. B. C., Casalino, G., Bartolini, G., Cannata, G., Veruggio, G., Canals, M., Smith, C., O'Brien, D. J., Pickett, M., Robinson, G., Jones, D., Scott, E., Ferrara, A., Angelleti, D., Coccoli, M., Bono, R., Virgili, P., Pallas, R., and Gracia, E., 1997, "AMADEUS: Advanced Manipulation for Deep Underwater Sampling," IEEE Rob. Autom. Mag., **4**(4), pp. 34–45.

[6] McMahan, W., Chitrakaran, V., Csencsits, M., Dawson, D. M., Walker, I. D., Jones, B. A., Pritts, M., Dienno, D., Grissom, M., and Rahn, C. D., 2006, "Field Trials and Testing of the OctArm Continuum Manipulator," IEEE International Conference on Advanced Robotics (ICAR), Orlando, FL, pp. 2336–2341.

[7] Hirose, S., 1993, *Biologically Inspired Robots, Snake-Like Locomotors and Manipulators*, Oxford University Press, New York.

[8] Breedveld, P., and Hirose, S., 2001, "Development of the Endo-periscope for Improvement of Depth Perception in Laparoscopic Surgery," ASME Design Engineering Technical Conferences Computers and Information in Engineer-

ing Conference, Pittsburgh, PA, p. 7.
[9] Peirs, J., Reynaerts, D., Van Brussel, H., De Gersem, G., and Tang, H.-W., 2003, "Design of an Advanced Tool Guiding System for Robotic Surgery," IEEE International Conference on Robotics and Automation (ICRA), Taipei, Taiwan, pp. 2651–2656.
[10] Gravagne, I. A., and Walker, I. D., 2000, "On the Kinematics of Remotely-Actuated Continuum Robots," IEEE International Conference on Robotics and Automation (ICRA), San Francisco, CA, pp. 2544–2550.
[11] Simaan, N., Taylor, R. H., and Flint, P., 2004, "A Dexterous System for Laryngeal Surgery," IEEE International Conference on Robotics and Automation (ICRA), New Orleans, LA, pp. 351–357.
[12] Patronik, N. A., Zenati, M. A., and Riviere, C. N., 2004, "Crawling on the Heart: A Mobile Robotics Device for Minimally Invasive Cardiac Interventions," International Conference on Medical Image Computing and Computer-Assisted Intervention (MICCAI), St. Malo, France, pp. 9–16.
[13] Suzumori, K., Iikura, S., and Tanaka, H., 1991, "Development of Flexible Microactuator and Its Applications to Robotic Mechanisms," IEEE International Conference on Robotics and Automation (ICRA), Sacramento, CA, pp. 1622–1627.
[14] Haga, Y., Esashi, M., and Maeda, S., 2000, "Bending, Torsional and Extending Active Catheter Assembled Using Electroplating," International Conference on Micro Electro Mechanical Systems (MEMS), Miyazaki, Japan, pp. 181–186.
[15] Dario, P., Paggetti, C., Troisfontaine, N., Papa, E., Ciucci, T., Carrozza, M. C., and Marcacci, M., 1997, "A Miniature Steerable End-Effector for Application in an Integrated System for Computer-Assisted Arthroscopy," IEEE International Conference on Robotics and Automation (ICRA), Albuquerque, NM, pp. 1573–1579.
[16] Asari, V. K., Kumar, S., and Kassim, I. M., 2000, "A Fully Autonomous Microrobotic Endoscopy System," J. Intell. Robotic Syst., **28**(4), pp. 325–341.
[17] Patronik, N. A., Ota, T., Zenati, M. A., and Riviere, C. N., 2006, "Improved Traction for a Mobile Robot Traveling on the Heart," Annual International Conference of the IEEE Engineering in Medicine and Biology Society (EMBS), New York, NY, pp. 339–342.
[18] Webster, R. J., Romano, J. M., and Cowan, N. J., 2009, "Mechanics of Precurved-Tube Continuum Robots," IEEE Trans. Robot., **25**(1), pp. 67–78.
[19] Sears, P., and Dupont, P. E., 2007, "Inverse Kinematics of Concentric Tube Steerable Needles," IEEE International Conference on Robotics and Automation, Rome, Italy, pp. 1887–1892.
[20] Minhas, D. S., Engh, J. A., Fenske, M. M., and Riviere, C. N., 2007, "Modeling of Needle Steering Via Duty-Cycled Spinning," Annual International Conference of the IEEE Engineering in Medicine and Biology Society (EMBS), Cité Internationale, Lyon, France, pp. 2756–2759.
[21] Alterovitz, R., Branicky, M., and Goldberg, K., 2008, "Motion Planning Under Uncertainty for Image-Guided Medical Needle Steering," Int. J. Robot. Res., **27**(11–12), pp. 1361–1374.
[22] Gravagne, I. A., and Walker, I. D., 2002, "Manipulability, Force and Compliance Analysis for Planar Continuum Manipulators," IEEE Trans. Rob. Autom., **18**(3), pp. 263–273.
[23] Gravagne, I. A., Rahn, C. D., and Walker, I. D., 2003, "Large Deflection Dynamics and Control for Planar Continuum Robots," IEEE/ASME Trans. Mechatron., **8**(2), pp. 299–307.
[24] Jones, B. A., and Walker, I. D., 2006, "Kinematics for Multisection Continuum Robots," IEEE Trans. Rob. Autom., **22**(1), pp. 43–55.
[25] Simaan, N., Taylor, R., and Flint, P., 2004, "High Dexterity Snake-like Robotic Slaves for Minimally Invasive Telesurgery of the Upper Airway," International Conference on Medical Image Computing and Computer-Assisted Intervention (MICCAI), St. Malo, France, pp. 17–24.
[26] Li, C., and Rhan, C. D., 2002, "Design of Continuous Backbone, Cable-Driven Robots," ASME J. Mech. Des., **124**, pp. 265–271.
[27] Nemat-Nasser, S., and Guo, W.-G., 2006, "Superelastic and Cyclic Response of NiTi SMA at Various Strain Rates and Temperatures," Mech. Mater., **38**(5–6), pp. 463–474.
[28] Kimball, C., and Tsai, L.-W., 2002, "Modeling of Flexural Beams Subjected to Arbitrary End Loads," ASME J. Mech. Des., **124**, pp. 223–235.
[29] Mitchell, T. P., 1959, "The Nonlinear Bending of Thin Rods," ASME J. Appl. Mech., **26**, pp. 40–43.
[30] Howell, L. L., and Midha, A., 1995, "Parametric Deflection Approximations for End-Loaded, Large-Deflection Beams in Compliant Mechanisms," ASME J. Mech. Des., **117**, pp. 156–165.
[31] Su, H.-J., 2009, "A Pseudorigid-Body 3R Model for Determining Large Deflection of Cantilever Beams Subject to Tip Loads," ASME J. Mech. Rob., **1**(2), p. 021008.
[32] Awtar, S., Slocum, A. H., and Sevincer, E., 2007, "Characteristics of Beam-Based Flexure Modules," ASME J. Mech. Des., **129**(6), pp. 625–639.
[33] Byrd, P. F., and Friedman, M. D., 1971, *Handbook of Elliptic Integrals for Engineers and Scientists*, Springer-Verlag, New York.
[34] Nocedal, J., and Wright, S. J., 2006, *Numerical Optimization*, Springer, New York.
[35] Han, S. P., 1977, "A Globally Convergent Method for Nonlinear Programming," J. Optim. Theory Appl., **22**(3), pp. 297–309.
[36] Powell, M. J. D., 1978, "A Fast Algorithm for Nonlinearly Constrained Optimization Calculations," Numerical Analysis (Lect. Notes Math.), **630**, pp. 144–157.
[37] Xu, K., and Simaan, N., 2008, "An Investigation of the Intrinsic Force Sensing Capabilities of Continuum Robots," IEEE Trans. Robot., **24**(3), pp. 576–587.
[38] Simaan, N., 2005, "Snake-Like Units Using Flexible Backbones and Actuation Redundancy for Enhanced Miniaturization," IEEE International Conference on Robotics and Automation (ICRA), Barcelona, Spain, pp. 3012–3017.
[39] Kapoor, A., Simaan, N., and Taylor, R. H., 2005, "Suturing in Confined Spaces: Constrained Motion Control of a Hybrid 8-DoF Robot," International Conference on Advanced Robotics (IACR), Seattle, pp. 452–459.
[40] Horn, B., 1986, *Robot Vision*, MIT Press, Boston.
[41] Xu, K., and Simaan, N., 2006, "Actuation Compensation for Flexible Surgical Snake-like Robots With Redundant Remote Actuation," IEEE International Conference on Robotics and Automation (ICRA), Orlando, FL, pp. 4148–4154.
[42] Simaan, N., Xu, K., Kapoor, A., Wei, W., Kazanzides, P., Flint, P., and Taylor, R. H., 2009, "Design and Integration of a Telerobotic System for Minimally Invasive Surgery of the Throat," Int. J. Robot. Res., **28**(9), pp. 1134–1153.
[43] Timoshenko, S. P., and Gere, J. M., 1961, *Theory of Elastic Stability*, McGraw-Hill, New York.
[44] Aristizábal-Ochoa, J. D., 2004, "Large Deflection Stability of Slender Beam-Columns With Semirigid Connections: Elastica Approach," J. Eng. Mech., **130**(3), pp. 274–282.